Geophysical Research Letters

Supporting Information for

Accelerating Seafloor Uplift of Submarine Caldera near Sofugan Volcano, Japan, Resolved by Distant Tsunami Recordings

Tatsuya Kubota[1], Osamu Sandanbata[2], Tatsuhiko Saito[1], and Takanori Matsuzawa

[1]National Research Institute for Earth Science and Disaster Resilience, Tsukuba, Japan

[2]Earthquake Research Institute, the University of Tokyo, Tokyo, Japan

Contents of this file

Introduction

Text S1 explains the T-phase signals recorded in the onshore and offshore seismometers. In Texts S2, we describe the detailed procedure of the inversion analysis for the sea-surface height distribution. The effect of the seawater column on the tsunami excitation is discussed in Text S3.

Figure S1 shows a comparison of the tsunami waveforms during this event and the 2015 Torishima earthquake, and their epicenter locations are shown in Figure S2. Figure S3 shows the T-phase signals confirmed in the onshore and offshore seismometers. Figure S4 is the schematic illustration of the inversion analysis in the present study. The target area for the tsunami simulation is shown in Figure S5. Figure S6 shows the trade-off of the weights of the constraint, which were used to determine the optimum weights. Figures S7 and S8 are the inversion results without considering the dispersion effect in the tsunami. The inversion result imposing the non-negative constraint is shown in Figures S9 and S10. Figure S11 evaluates the effect of the seawater column on the tsunami generation in various source sizes. Figure S12 compares the observed tsunami waveforms with the simulated ones calculated from the modeling to determine the seafloor uplift amount. Figure S13 shows the amount of the seafloor uplift and total displaced volume assuming various modeling parameters. Figure S14 is the nearby onshore seismograms due to each of the events.

Text S1.

Based on the analyses of the T-phase signals in the DONET OBP data, Sandanbata et al. (2024) identified 13 significant events during the sequence. These 13 events correspond to the earthquakes listed in the USGS catalog (Events 01 to 13 in Table 1). However, the T-phase signal associated with Event 14 at 21:26 was not identified. To confirm whether the T-phase signal from Event 14 was recorded, we inspected onshore and offshore seismometers around Japan (Figure S3). Supposing the propagation velocity of the T-phases as 1.5 km/s, we calculate the theoretical arrival times of the T-phases from each event (dashed lines in Figure S3) and compare the arrival of the wave signals at the seismometers. For example, the expected travel times to nearby onshore broadband seismometers at Aogashima Island (AOGF, ~300 km from the epicenter) and Ogasawara Island (OSWF) (~350 km), are Δt ~200 s and Δt ~230 s, respectively (blue and green bars in Figure S3a), which are consistent with the arrival timings of the T-phases from Events 01 to 13. At the expected T-phase arrival time from Event 14, we can confirm the arrival of the wave packets, although its amplitude is smaller than the other events.

Text S2.

We here describe the methodology and strategy of the inversion analysis for the sea-surface displacement in each event (Figures 2 and 3). We express the generation and propagation of the tsunami by using the two-dimensional liner dispersive tsunami wave equation with the Cartesian coordinates (e.g., Saito, 2019), as:

$$\frac{\partial \eta(\mathbf{x},t)}{\partial t} = -\nabla \cdot (h\bar{\mathbf{v}}) + \dot{\eta}^s(\mathbf{x},t) \tag{S1}$$

and

$$\frac{\partial \bar{\mathbf{v}}(\mathbf{x},t)}{\partial t} = -g_0 \nabla \eta + \frac{1}{3} h(\mathbf{x}) \frac{\partial}{\partial t} \nabla\big(\nabla \cdot (h\bar{\mathbf{v}})\big) \tag{S2}$$

where $\eta = \eta(\mathbf{x}, t)$ is the sea-surface height change, $\bar{\mathbf{v}} = \bar{\mathbf{v}}(\mathbf{x}, t)$ is the horizontal velocity averaged over the water depth, $h = h(\mathbf{x})$ is the water depth, and g_0 is the gravitational acceleration. The term $\dot{\eta}^s = \dot{\eta}^s(\mathbf{x}, t)$ is the velocity of the sea-surface height change generated by the events:

$$\dot{\eta}^s(\mathbf{x},t) = \sum_{k=1}^{N_t} \eta_0^{(k)}(\mathbf{x}) \delta(t - T_k) \tag{S3}$$

where $\eta_0^{(k)}(\mathbf{x})$ is the sea-surface height change due to the k-th event and N_t is the total number of events. The k-th event occurs at the time $t = T_k$ (T_k is the origin time of the k-th event).

In a typical inversion analysis to estimate the spatiotemporal evolution involving the multiple subevents, the multiple source elements are assumed in the time domain with uniform temporal intervals (i.e., $T_k = 0, \Delta T, 2\Delta T, \ldots N_t \Delta T$). However, in the present case, the total time length during the event sequence is too long (approximately ~90 min), and thus the number of the source elements should be too large. Therefore, the inversion problem should be unstable if we use the same way as the typical inversion analysis. Another approach is the deconvolution-based approach (e.g., Kikuchi & Kanamori, 1982), which repetitively estimates the best-fit point source (location and timing) and subtracts the contribution of the best-fit

model from the observation. However, this approach may cause a trade-off between the location and the timing because of the long wavelength of the tsunami. To stably solve the inversion problem, we utilize the USGS catalog as prior information for the event origin times. More specifically, we set N_t in Equation (S3) as N_t= 14 and assume the origin times of each event (T_k) as those determined by USGS (Table 1; Figure S4).

We suppose that the waveforms at the n-th OBP located at $\mathbf{x}_n = (x_n, y_n)$, $p_n(t) = \rho_0 g_0 \eta(\boldsymbol{x}_n, t)$ (ρ_0: the seawater density, ~1.03 g/cm^3) can be represented by a linear superposition of tsunami waveforms due to unit source elements of the sea-surface displacement, as:

$$p_n(t) = \sum_{i=1}^{N_x} \sum_{j=1}^{N_y} \sum_{k=1}^{N_t} m^{(i,j,k)} G_n^{(i,j)}(t - T_k), \tag{S4}$$

where the parameter $m^{(i,j,k)}$ is the displacement amplitude of the (i, j, k)-th unit source element of the sea-surface displacement, which is to be estimated in the linear inversion problem, and N_x and N_y are the numbers of the unit source elements in the spatial domain along the x- and y-directions, respectively. Note that the total number of the unknown parameters is $N = N_x \times N_y \times N_t$. $G_n^{(i,j)}(t - T_k)$ is a time series of the sea-surface height change at the location $\mathbf{x}_n$ due to the (i, j, k)-th unit source element (hereafter referred to as the Green's function). We assume the (i, j, k)-th Green's function is excited by the displacement of the unit source element of sea-surface height $\eta_{\mathrm{s}}^{(i,j,k)}(\mathbf{x}, t)$. The time history of $\eta_{\mathrm{s}}^{(i,j,k)}(\mathbf{x}, t)$ is expressed as

$$\eta_{\mathrm{s}}^{(i,j,k)}(\mathbf{x}, t) = \eta_1^{(i,j)}(\mathbf{x}) H(t - T_k), \tag{S5}$$

where $\eta_1^{(i,j)}(\mathbf{x})$ is the spatial distribution of the (i, j)-th static sea-surface displacement (hereafter, referred to as the spatial basis function) and $H(t)$ is the Heaviside step function. We note that $\eta_0^{(k)}(\mathbf{x})$ in Equation (S3) can be expressed using $\eta_1^{(i,j)}(\mathbf{x})$, as:

$$\eta_0^{(k)}(\mathbf{x}) = \sum_{i=1}^{N_x} \sum_{j=1}^{N_y} m^{(i,j,k)} \eta_1^{(i,j)}(\mathbf{x}). \tag{S6}$$

We also note that the total static sea-surface displacement, $\eta_{\mathrm{total}}(\mathbf{x})$, can be expressed as:

$$\eta_{\mathrm{total}}(\mathbf{x}) = \sum_{k=1}^{N_t} \eta_0^{(k)}(\mathbf{x}) = \sum_{i=1}^{N_x} \sum_{j=1}^{N_y} \sum_{k=1}^{N_t} m^{(i,j,k)} \eta_1^{(i,j)}(\mathbf{x}). \tag{S7}$$

To calculate the Green's function $G_n^{(i,j,k)}(t)$ in Equation (S4), we suppose the shape of the spatial basis function $\eta_1^{(i,j)}(\mathbf{x})$ as:

$$\eta_1^{(i,j)}(\mathbf{x}) = \left[\frac{1}{2} + \frac{1}{2}\cos\left(\frac{2\pi(x - x_i)}{L_x}\right)\right]\left[\frac{1}{2} + \frac{1}{2}\cos\left(\frac{2\pi(y - y_j)}{L_y}\right)\right]$$
$$\text{for} \quad x_i - \frac{L_x}{2} \le x \le x_i + \frac{L_x}{2},\ y_j - \frac{L_y}{2} \le y \le y_j + \frac{L_y}{2}. \tag{S8}$$

Here, $\mathbf{x}_i = (x_i, y_j)$ is the center location of the (i, j)-th basis function, and L_x and L_y are the spatial dimensions of the basis functions along x- and y-directions, respectively. We suppose

$L_x = L_y$ = 6 km in this study, and each of them overlaps with the adjacent ones with a spatial interval of 3 km. We set the number of the unit sources asN_x = 9 and N_y = 8 (i.e., the total number of the unit source is $N_{xy} = N_x \times N_y$ = 72, and the analytical area is 30 km × 27 km; gray rectangle in Figure 1e). Then, the tsunami height is numerically calculated by solving the linear dispersive tsunami equation (e.g., Saito, 2019). We use the GEBCO 2020 bathymetry data (GEBCO Bathymetric Complication Group 2020, 2020) for the numerical simulation (Figure S5). The original resolution of the GEBCO 2020 is 30 min (~0.5 km), but we interpolate it to the spatial interval of $\Delta x = \Delta y$ = 1 km, because of the computational cost. The total number of the computational grids is 1,601 × 1,601. The time step interval of the simulation is Δt = 1 s, and the total number of the simulation step is N_{step} = 7,200. Then we obtain the Green's functions as the tsunami waveforms at each OBP location, assuming a 1 cm of the sea-surface height change is equivalent to a 1 hPa of the seafloor pressure change. Finally, we applied the same bandpass filter as that used in the data processing to the Green's functions.

We solve the following normal equation as an inversion problem, to estimate the amount of the displacements of each unit source element (the parameter $m^{(i,j,k)}$ in Equation (S4)).

$$\begin{pmatrix} \mathbf{p} \\ \mathbf{0} \\ \mathbf{0} \end{pmatrix} = \begin{pmatrix} \mathbf{G} \\ \alpha\mathbf{S} \\ \beta\mathbf{E} \end{pmatrix} \mathbf{m} \tag{S9}$$

where $\mathbf{p}$ is the data vector, consisting of the observed data, $p_n(t)$, the matrix $\mathbf{G}$ consists of the Green's function. The original sampling of the DONET and S-net data is 10 Hz, but we decimated to 0.1 Hz after the bandpass filtering to the raw data in this inversion, to save computational time. The time window used for the inversion analysis is set as 14,400 s from the origin time of Event 01, which includes the main part of the tsunamis. Based on the visual inspection of the tsunami waveforms, we used the OBP stations which recorded the tsunamis (station names are shown in blue text in Figure 2). The vector $\mathbf{m}$ consists of $m^{(i,j,k)}$, which is to be solved (the number of the unknown parameter is $N = N_x \times N_y \times N_t$ = 1,008). To stabilize the inversion, we impose the constraints of the spatial smoothing (represented by the matrix $\mathbf{S}$) and the spatial damping (the matrix $\mathbf{E}$ consists of the identity matrix). Their weights α and β are determined based on the trade-off between the weight and the variance reduction (VR) (Figure S6), defined as:

$$\mathrm{VR} = \left(1 - \frac{\sum_n \left(p_n^{\mathrm{obs}} - p_n^{\mathrm{cal}}\right)^2}{\sum_n {p_n^{\mathrm{obs}}}^2}\right) \times 100\ (\%). \tag{S10}$$

where p_n^{obs} and p_n^{cal} are the n-th data of the observed and calculated waveforms.

To evaluate the robustness of the inversion, we further conduct some additional inversion analyses (Figures S7–S10). We first conduct the inversion the Green's functions without considering the tsunami dispersion effect (e.g., Saito, 2019) to evaluate the importance of the dispersion effect (Figures S7 and S8). The estimated tsunami source showed the sea-surface subsidence for (Figure S7), but this model did not reproduce the observed waveforms well (VR = 28 %, Figure S8). From this low VR, we rejected this model and concluded that it is necessary to consider the dispersion effect to appropriately estimate the tsunami source.

We also conduct the inversion imposing the constraint that does not allow the sea-surface subsidence (i.e., non-negative constraint, Lawson & Hanson, 1974), to evaluate the robustness of the subsidence for each event surrounding the main uplift regions (Figures S9

and S10). The other settings for the inversion are all the same as the original one. The locations of the uplift are estimated at almost the same locations to the original result, and the agreement of the waveforms between the observation and simulation changed little (VR = 53 %). We cannot conclude whether this subsidence was real or just an artifact at this time. To better resolve the tsunami source, it should be necessary to use the shorter-period tsunami components (< 100 s, Sandanbata, Watada et al. 2021) or the seismic waves (Sandanbata et al., 2022). But we do not discuss it in detail but do in our next work.

Text S3.

We evaluate the effect and importance of the spatial smoothing effect due to the seawater layer (Kajiura, 1963) in the present case (Figure S11).

Following the discussion of Saito and Furumura (2009), we assume an isotropic distribution of the seafloor displacement to discuss the tsunami generation process in terms of the source dimension and seawater depth. The final vertical displacement at the seafloor is assumed to be given by a Gaussian function as:

$$d(\mathbf{x}) = D_0 \exp\left[-\frac{(x-x_0)^2+(y-y_0)^2}{a^2}\right] \quad \text{(S11)}$$

where D_0 and a are the maximum height in the displacement (D_0 = 1 cm is assumed) and the source dimension characterizing the horizontal spatial scale. Based on a theoretical study by Saito and Furumura (2009), the relation between the sea-surface height distribution $\eta(x, y)$ caused by the seafloor deformation $d(x, y)$ is expressed as (Saito, 2019):

$$\eta(x,y) = \mathrm{F}^{-1}\left[\hat{\eta}\left(k_x, k_y\right)\right] = \mathrm{F}^{-1}\left[\frac{1}{\cosh k_0 h_0}\hat{d}\left(k_x, k_y\right)\right] \quad \text{(S12)}$$

where h_0 is the seawater depth (assumed to be constant), $\hat{\eta}\left(k_x, k_y\right)$ and $\hat{d}\left(k_x, k_y\right)$ are the 2-D Fourier transform of $\eta(x, y)$ and $d_z(x, y)$, respectively, and $\mathrm{F}^{-1}[\dots]$ is the 2-D inverse Fourier transform concerning the wavenumber $\left(k_x, k_y\right)$, and $k_0 = \sqrt{k_x^2 + k_y^2}$.

Based on the theoretical study of Saito and Furumura (2009), they pointed out that this filtering effect cannot be ignored if $k_0 h_0 > 0.5$. To visualize the effect of the depth filtering effect of Kajiura (1963) and quantitatively evaluate the necessity of this effect of the appropriate estimation of the amount of the seafloor vertical displacement, we calculate the sea-surface height distribution varying the spatial dimension of the source and the seawater depth (Figure S11). When we assume the narrow source dimension of a = 5 km, the impact on the spatial filtering effect cannot be negligible when the seawater depth is h_0 = 1.5 km, and the effect becomes stronger when the seawater depth is further deeper. On the other hand, if we assume the wide spatial source dimension such as a = 15 km, the effect of the depth filter can be negligibly small even at the water depth of h_0 = 2 km.

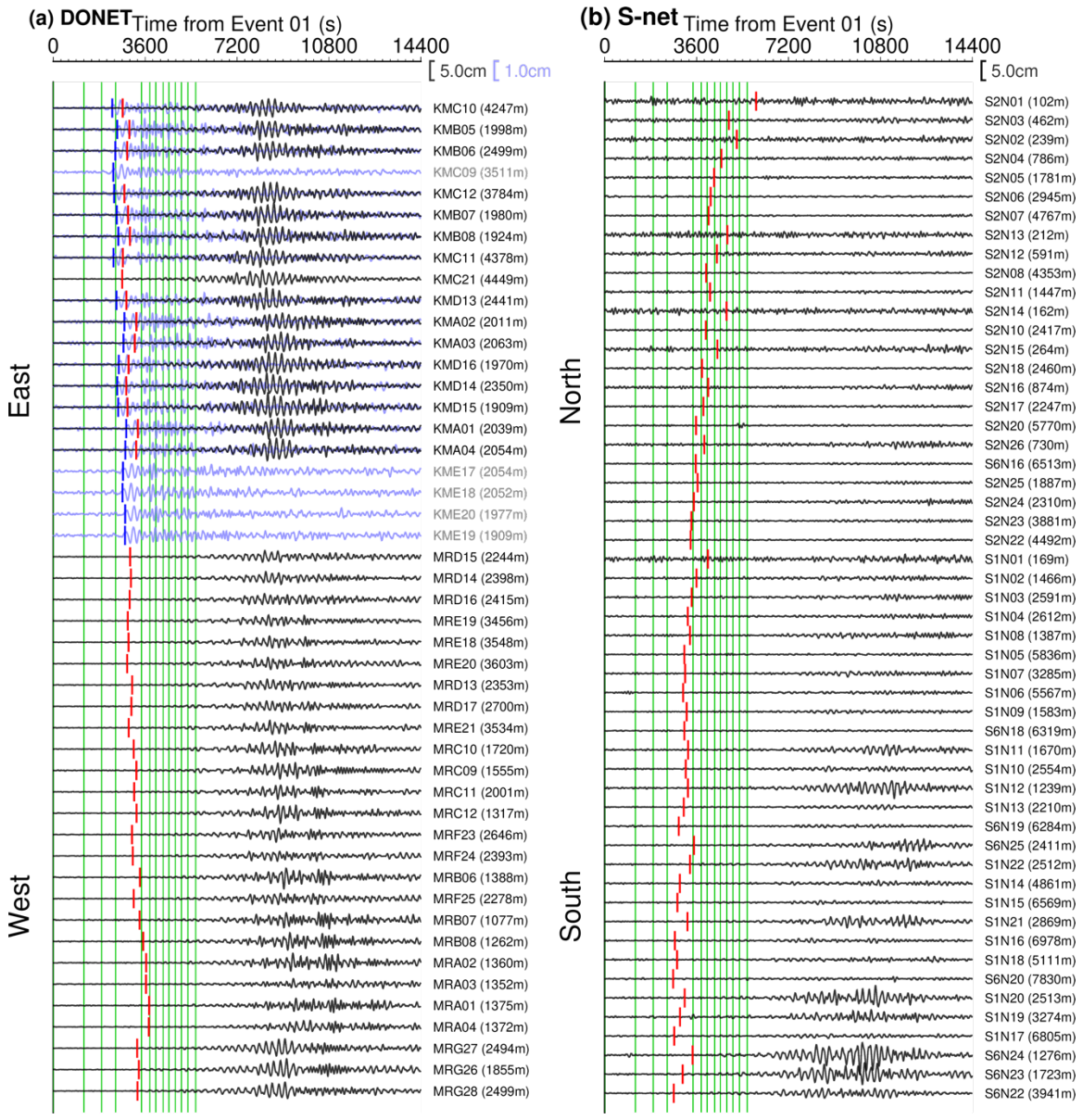

Figure S1. Tsunami waveforms recorded by the (a) DONET and (b) S-net pressure gauges (see Figure 1 for the station locations). The bandpass filter with the passband of 100–500 s was applied. In this figure, t = 0 denotes the origin time of the first event, Event 01 (19:53:46 on 08 October 2023 UTC). The red bars denote the expected tsunami arrival time (green contour lines in Figure S2). Green lines are the origin times of subsequent subevents. Blue traces and bars denote the tsunami waveforms recorded by DONET during the 2015 Torishima earthquake on May 2 and the expected arrivals of its tsunami (blue contour lines in Figure S2). Note that the vertical scales in the 2023 and 2015 events are different.

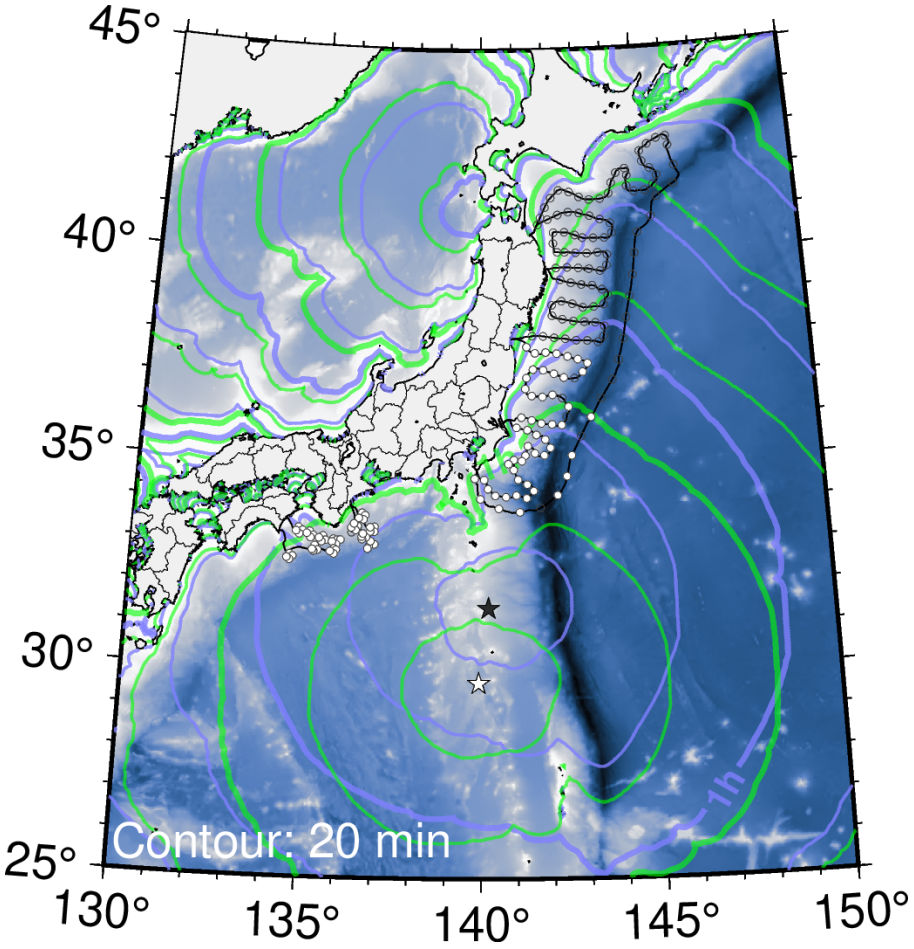

Figure S2. Comparison of the expected tsunami arrival times between the 2023 event (white star and green contours) and the 2015 earthquake near Torishima on 2 May 2015 (black star and blue contours). The contour interval is 20 min.

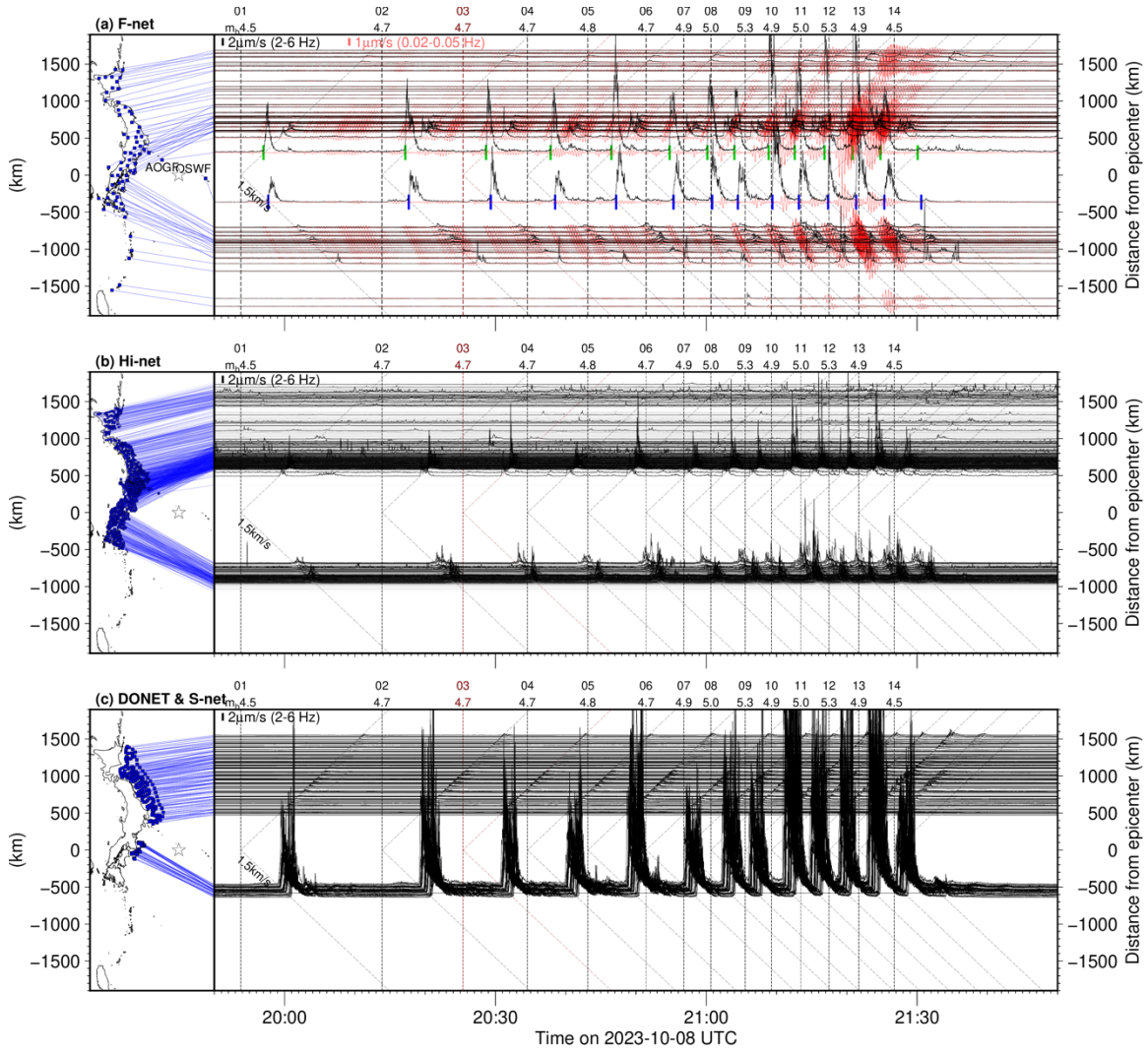

Figure S3. Envelope waveforms of onshore and offshore vertical seismograms during the event sequence. (a) The onshore seismograms from F-net (STS-1 broadband seismometers). (b) The onshore seismometers from Hi-net (1 Hz seismometers in borehole observatory). (c) The offshore seismometers from DONET (broadband seismometers) and S-net (1 Hz velocity seismometers). The black traces are the 2–6 Hz bandpass filtered waveforms, which is the dominant frequency band of T-phase (e.g., Okal, 2004), propagating at a velocity of ~1.5 km/s. Green and blue bars in Figure S3a denote the manually-picked arrival times of the T-phases, at the stations AOGF and OSWF, respectively (Table S1). Red traces in Figure S3a are the 0.02–0.05 Hz bandpass filtered waveforms, which are the dominant frequency of the body waves, propagating faster than the T-phases. For comparison, the approximate arrival times of T-phases are marked by dashed lines, calculated by $\Delta t = r/1.5$km, where r is the source-station distance. Note that the instrumental responses were not corrected.

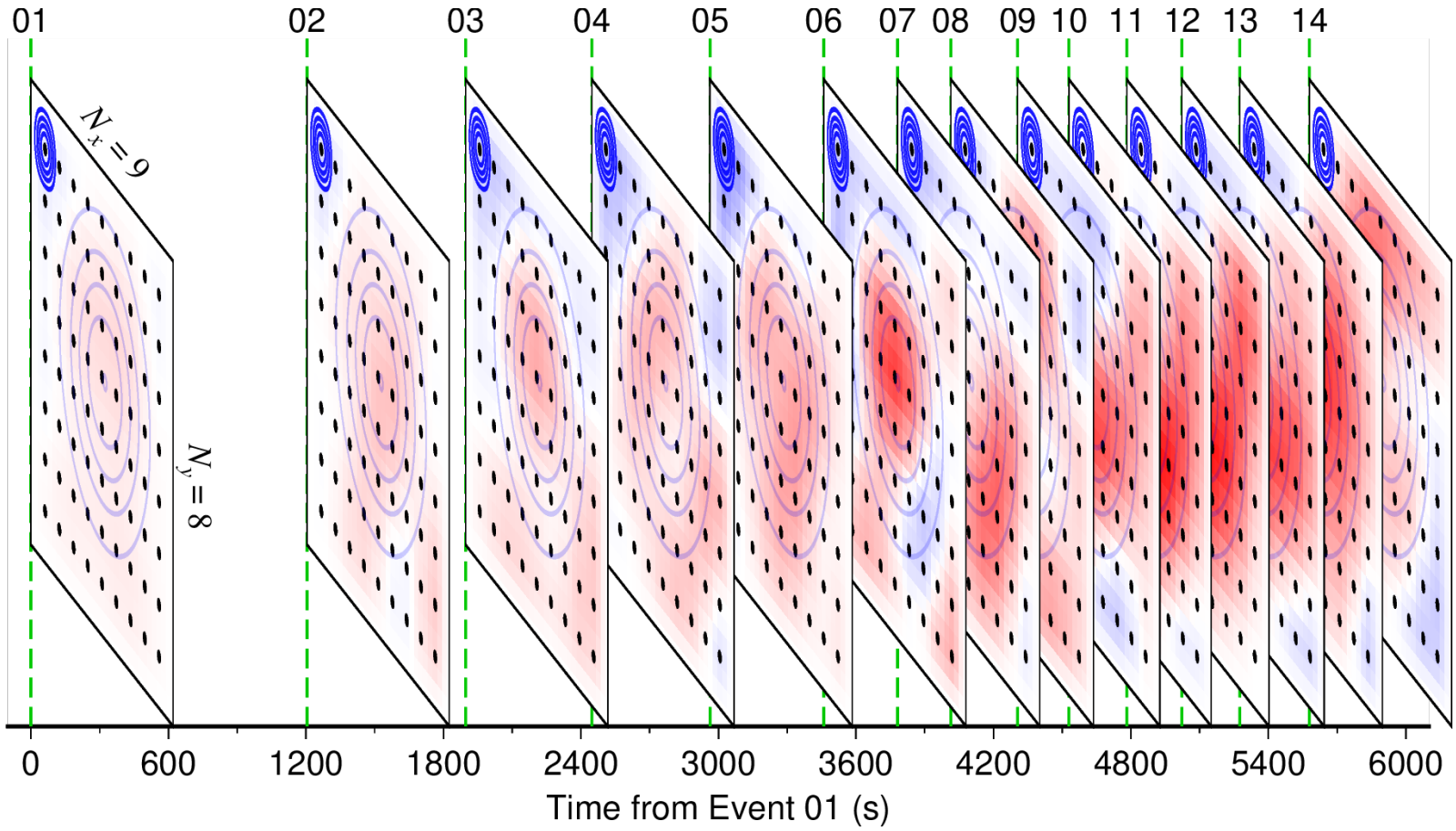

Figure S4. A schematic illustration of the inversion modeling. In the present study, the 9×8 unit source elements are distributed in the spatial domain, at each timing of the origin time of the events, Event 01, 02, …, and 14. Black dots denote the center locations of the distributed unit source, and the blue contours denote the sea-surface height change due to a unit source element at the top left.

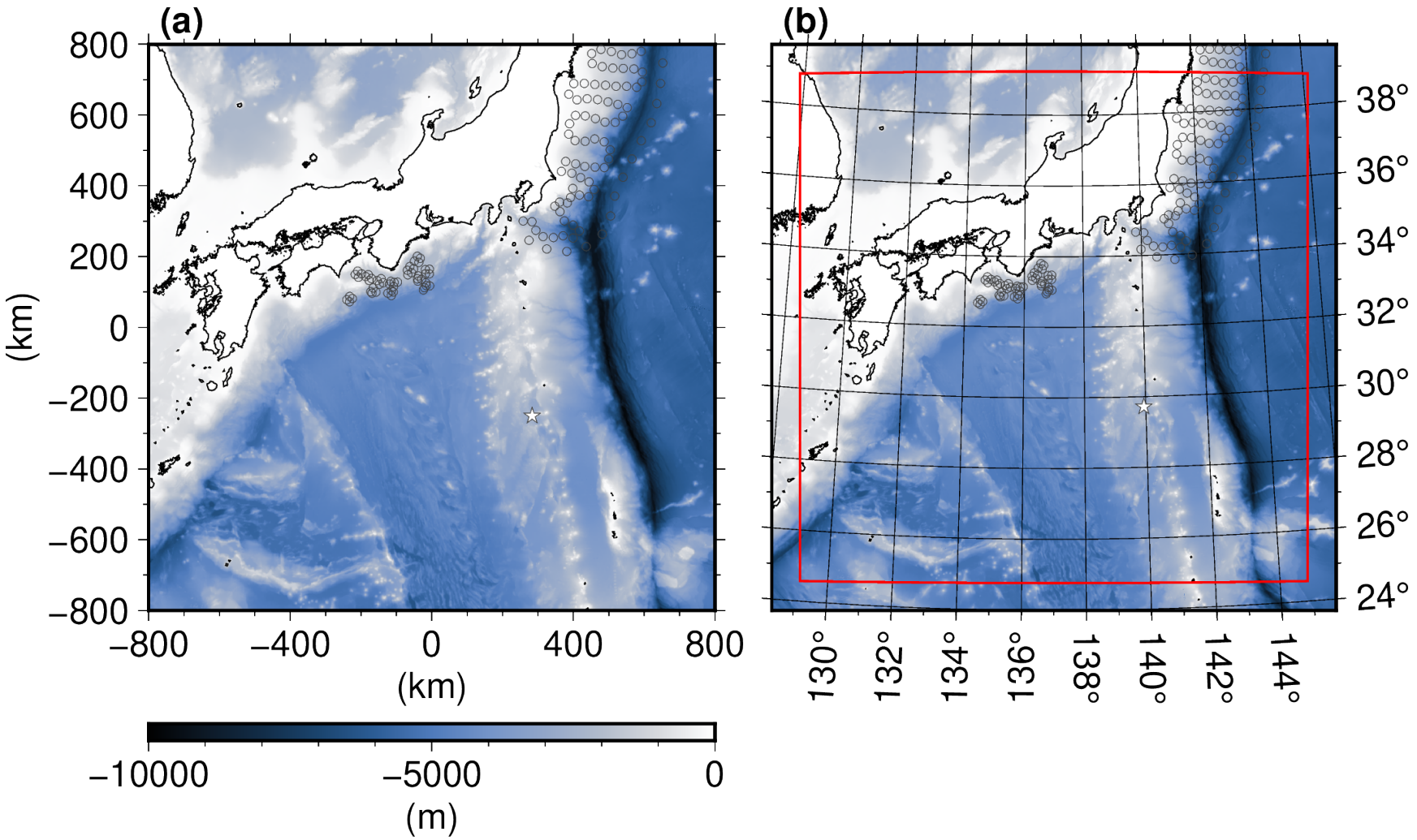

Figure S5. Seafloor bathymetry used for the tsunami simulation. (a) Simulation area in the Cartesian Coordinate. (b) The corresponding region in the Geographical Coordinate.

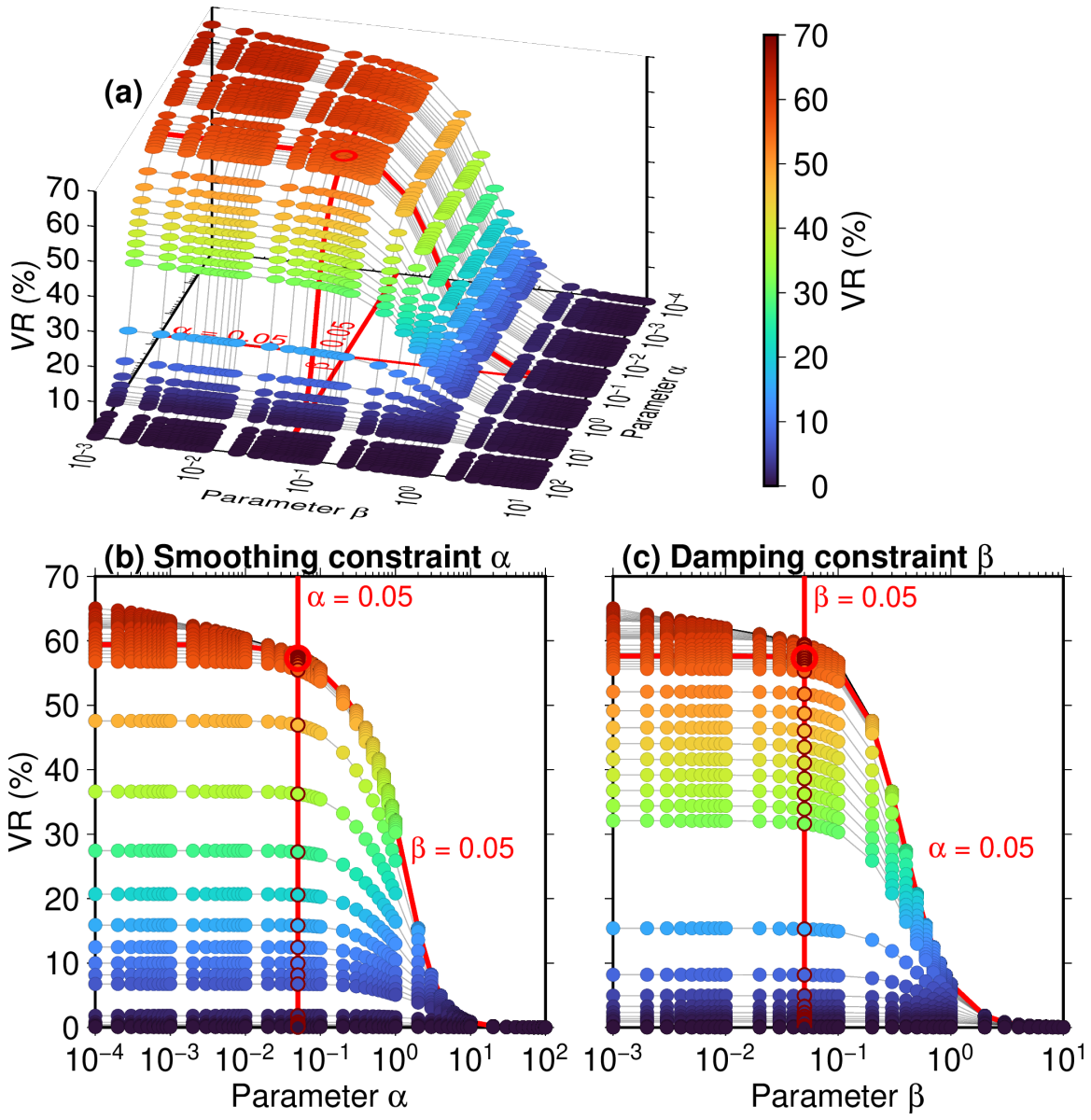

Figure S6. Trade-off curves of the smoothing and damping constraints in the inversion analysis. In this figure, we conducted the inversion analyses, varying the weights of the smoothing (α) and damping (β) to see the waveform fittings in terms of the VR values. (a) The whole results of the inversion trials. (b) VR values as a function of the parameter α. (c) VR values as a function of the parameter β. As a result, we determined the weight values as $\alpha = \beta = 0.5$, where the VR values begin to decrease.

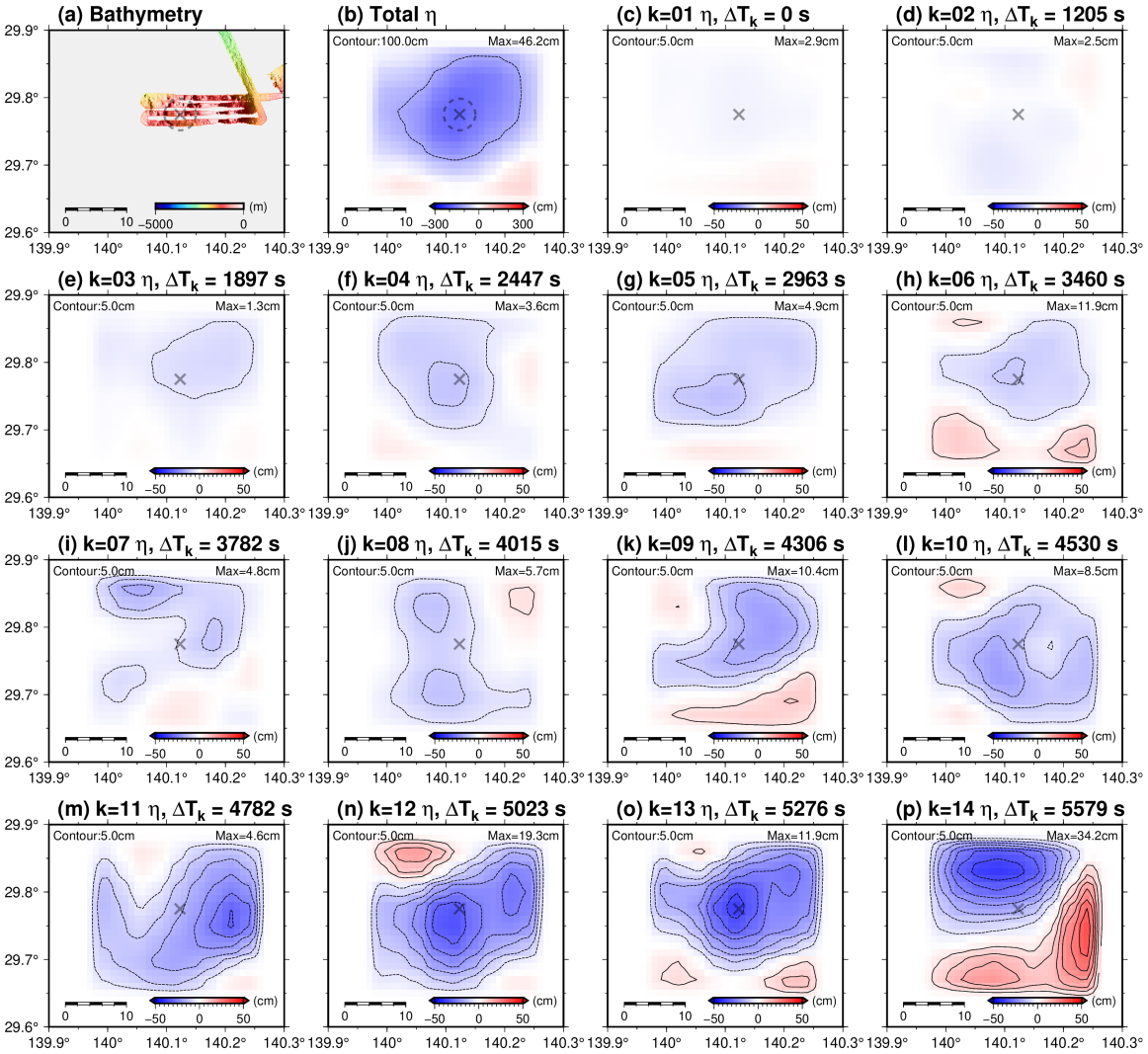

Figure S7. Distribution of the static vertical displacement of the sea-surface height, obtained by the inversion analysis without considering the tsunami dispersion effect. See Figure 3 for the detailed caption.

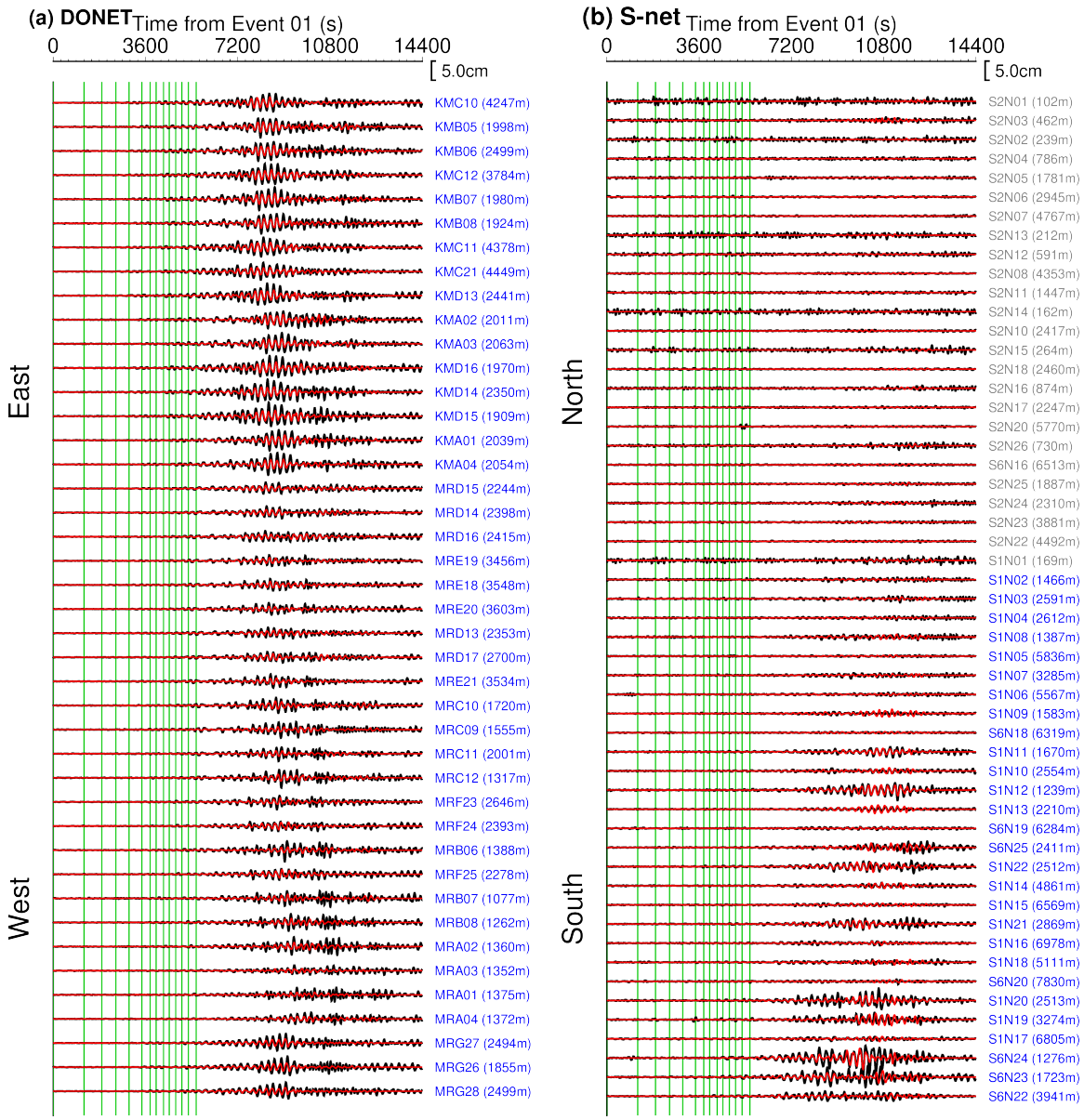

Figure S8. Comparison of the observed and simulated waveforms, obtained by the inversion analysis without considering the tsunami dispersion effect. See Figure 2 for the detailed caption.

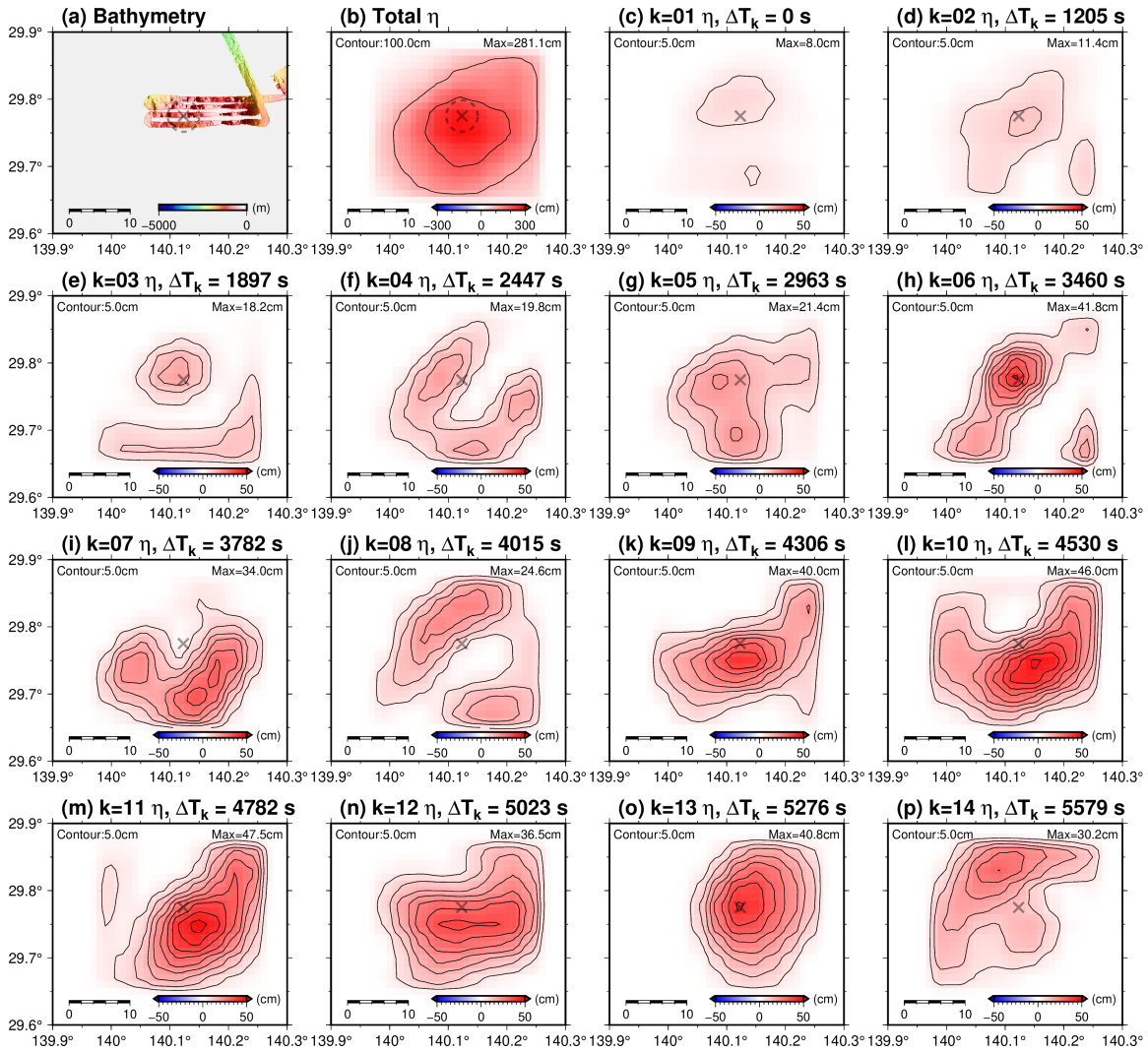

Figure S9. Distribution of the static vertical displacement of the sea-surface height, obtained by the inversion analysis imposing the non-negative constraint. See Figure 3 for the detailed caption.

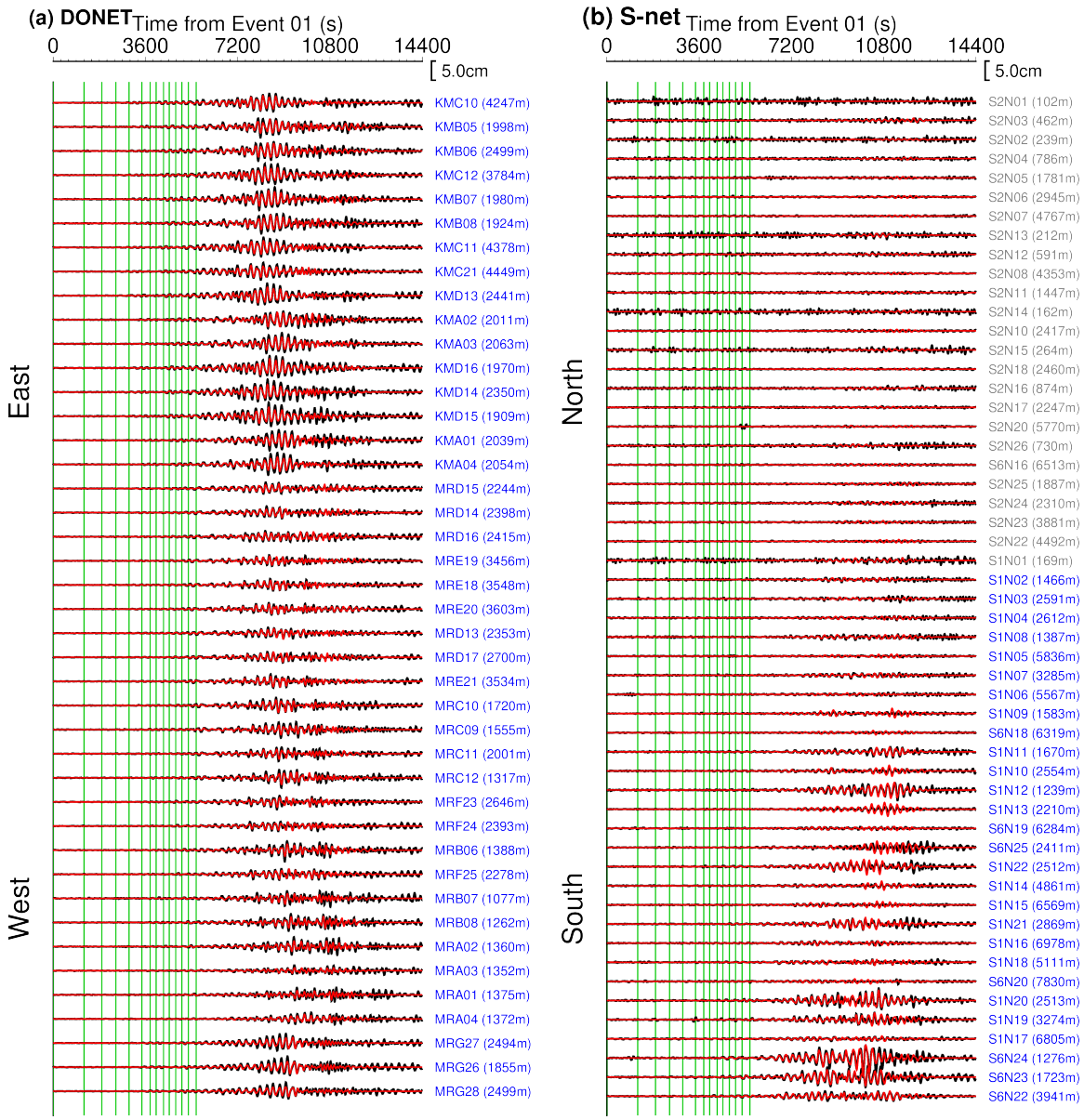

Figure S10. Comparison of the observed and simulated waveforms, obtained by the inversion analysis imposing the non-negative constraint. See Figure 2 for the detailed caption.

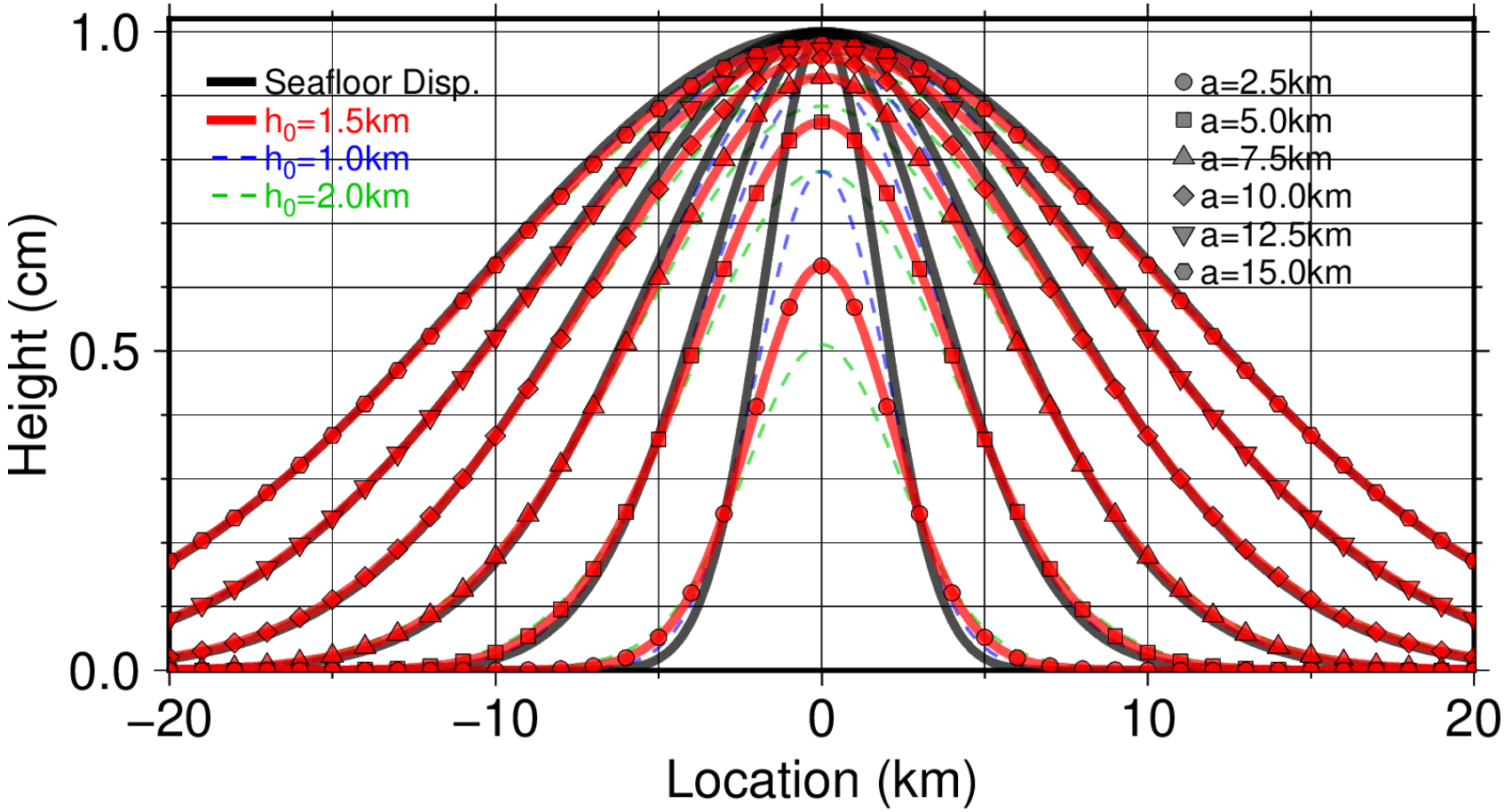

Figure S11. Cross section of sea-surface height distribution for various source sizes a = 2.5, 5.0, 7.5, and 10 km, at the seawater depth of h_0 = 1.0, 1.5, and 2.0 km. The seafloor deformation is shown by black lines, which are given by the Gaussian function of D_0 = 1 cm in Eq. (S11). For example, if we assume the source size of a = 5 km and h_0 = 1.5 km, the maximum amplitude of the sea-surface uplift (red line with circles) will reduce to ~85 % of D_0.

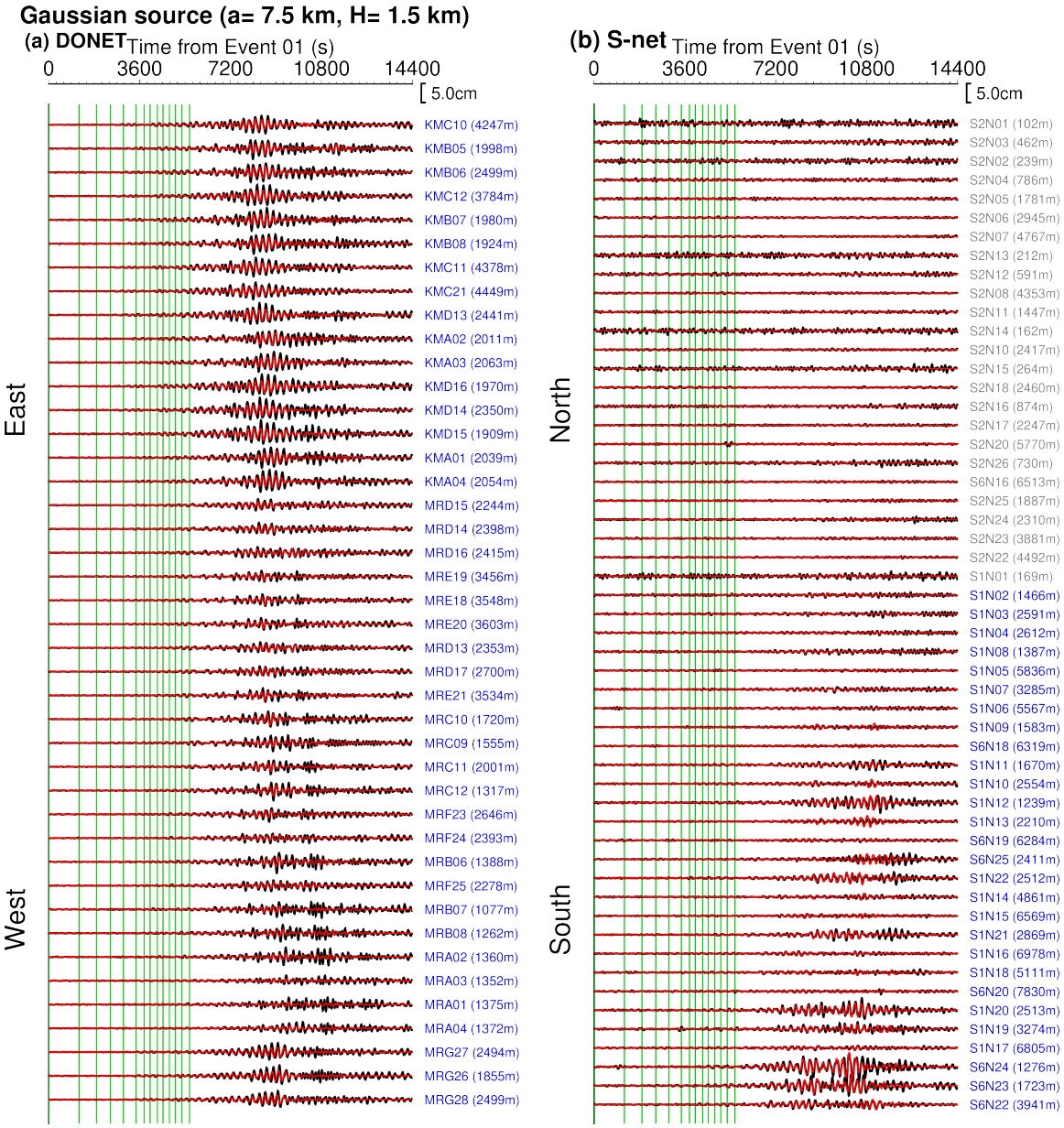

Figure S12. Comparison of the observed and simulated waveforms, obtained by the inversion analysis assuming the Gaussian unit source. See Figure 2 for the detailed caption.

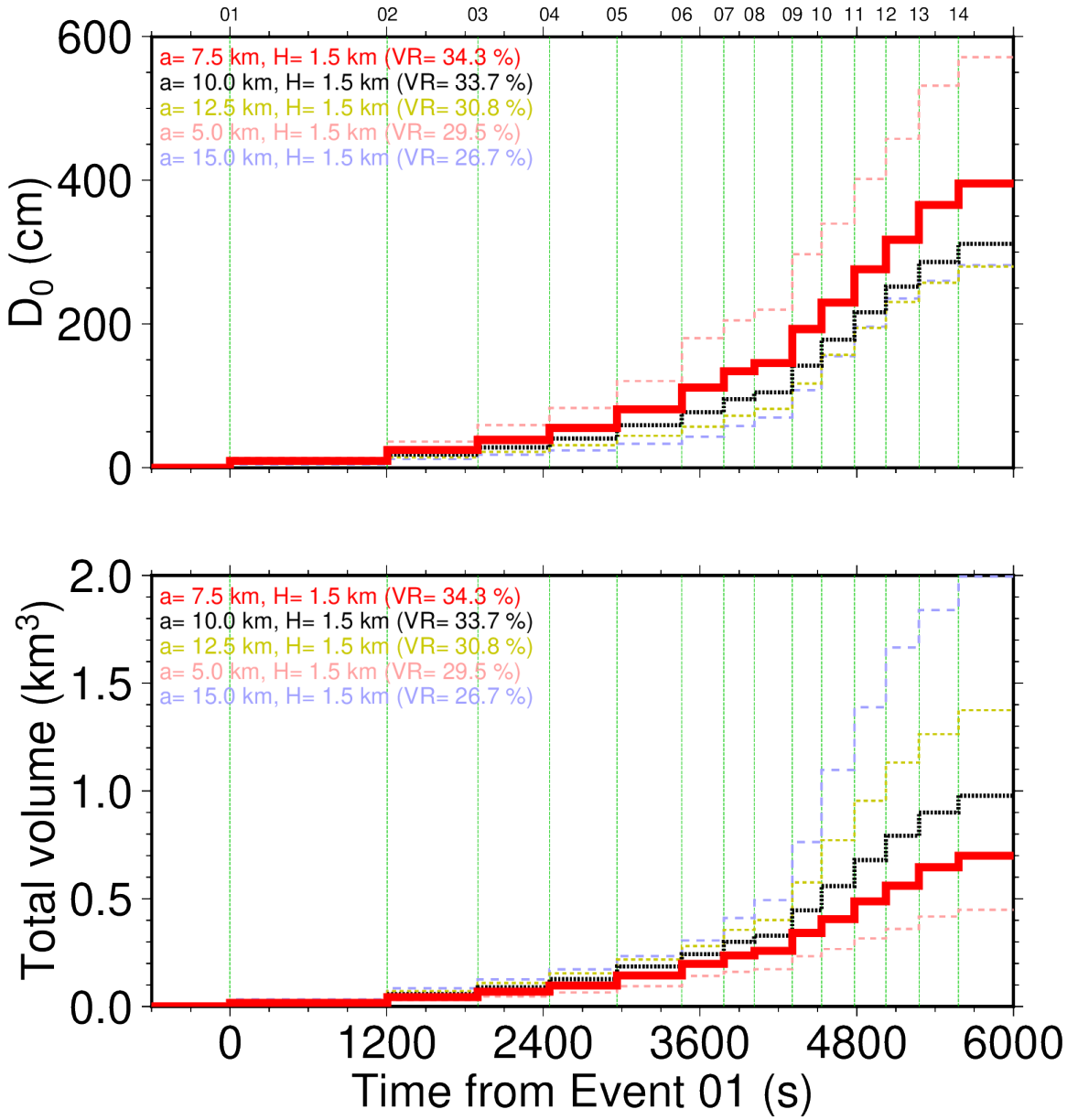

Figure S13. Comparison of the D_0 and total volume by different model parameters.

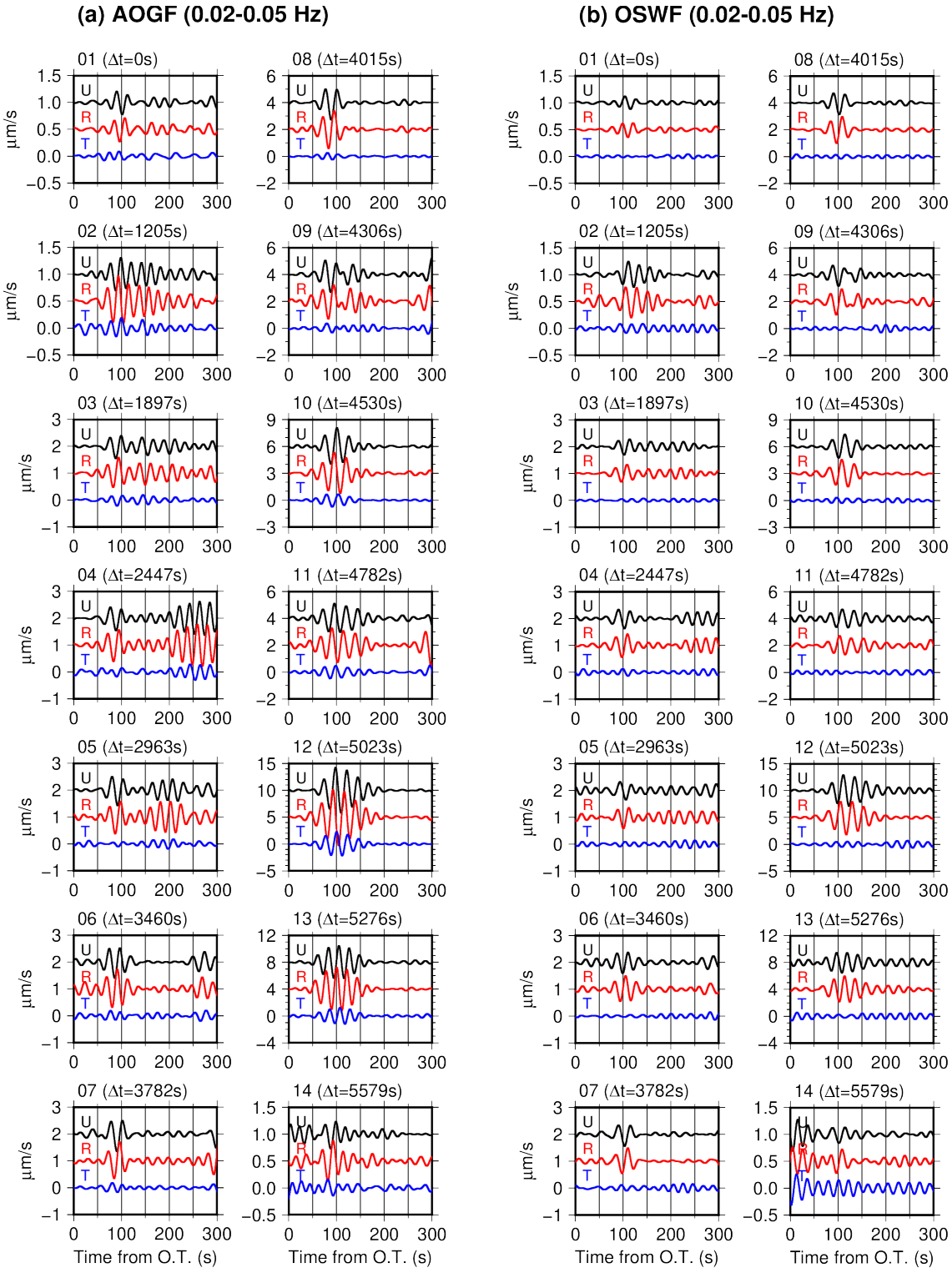

Figure S14. The F-net broadband seismograms from Events 01–14 at (a) AOGF and (b) OSWF. Black, red, and blue lines are the vertical, radial, and transverse components, respectively. The bandpass filter of 0.02–0.05 Hz is applied. It seems that the main wave packets arrive ~100 s from the origin time (O.T.). Some events have an impulse-like signal with a short duration, but others have relatively long duration, indicating the diversity of the seismic wave radiations.